



Morphology controlled synthesis of monodisperse cobalt hydroxide for supercapacitor with high performance and long cycle life

Yongfu Tang^{a,*}, Yanyan Liu^a, Shengxue Yu^a, Shichun Mu^b, Shaohua Xiao^c, Yufeng Zhao^a, Faming Gao^a

^a Hebei Key Laboratory of Applied Chemistry, College of Environmental and Chemical Engineering, Yanshan University, Qinhuangdao, Hebei 066004, China

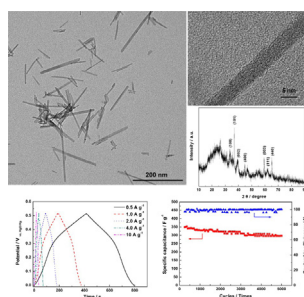
^b State Key Laboratory of Advanced Technology for Materials Synthesis and Processing, Wuhan University of Technology, Wuhan 430070, China

^c Key Laboratory of Catalysis and Materials Sciences of the State Ethnic Affairs Commission & Ministry of Education, College of Chemistry and Material Science, South-Central University for Nationalities, Wuhan 430074, China

HIGHLIGHTS

- Monodisperse cobalt hydroxide nanocubes and nanowires are synthesized.
- Morphology and size of $\text{Co}(\text{OH})_2$ are tuned by CTAB content and reaction time.
- $\text{Co}(\text{OH})_2$ nanowires electrode exhibits high performance and long cycle life.
- As-prepared asymmetric supercapacitor shows high voltage and energy density.

GRAPHICAL ABSTRACT



ARTICLE INFO

Article history:

Received 11 October 2013

Received in revised form

31 December 2013

Accepted 15 January 2014

Available online 23 January 2014

Keywords:

Cobalt hydroxide

Supercapacitor

Cubic nanocrystal

Nanowire

Asymmetric supercapacitor

ABSTRACT

A facile hydrothermal process with hexadecyltrimethyl ammonium bromide (CTAB) as the soft template is proposed to tune the morphology and size of cobalt hydroxide ($\text{Co}(\text{OH})_2$). Monodisperse β -phase $\text{Co}(\text{OH})_2$ nanowires with uniform size are obtained by controlling the CTAB content and the reaction time. Due to the uniform well-defined morphology and stable structure, the $\text{Co}(\text{OH})_2$ nanowires material exhibits high capacitive performance and long cycle life. The specific capacitance of the $\text{Co}(\text{OH})_2$ nanowires electrode is 358 F g^{-1} at 0.5 A g^{-1} , and even 325 F g^{-1} at 10 A g^{-1} . The specific capacitance retention is 86.3% after 5000 charge–discharge cycles at 2 A g^{-1} . Moreover, the asymmetric supercapacitor is assembled with $\text{Co}(\text{OH})_2$ nanowires and nitrite acid treated activated carbon (NTAC), which shows an energy density of 13.6 Wh kg^{-1} at the power density of 153 W kg^{-1} under a high voltage of 1.6 V, and 13.1 Wh kg^{-1} even at the power density of 1.88 kW kg^{-1} .

© 2014 Elsevier B.V. All rights reserved.

1. Introduction

Design and synthesis of nanocrystals with well-defined morphologies is significant in tailoring their properties [1]. Cobalt

hydroxide nanocrystals have attracted more attentions due to their application in supercapacitor [2–4], additive materials for alkaline secondary batteries [5,6] and electrochemical heterogeneous catalysis [7,8]. Morphology, nanostructured phase and particle size of cobalt hydroxide nanocrystals affect their conductive properties and specific capacitance in supercapacitor [9–11], as well as their catalytic activity for electrochemical reactions [12]. Furthermore, the cobalt hydroxides with well-

* Corresponding author. Tel.: +86 13780351724.

E-mail address: tangyongfu@ysu.edu.cn (Y. Tang).

defined morphologies are the precursors for the shape-controlled synthesis of cobalt oxides [13–16], which have been widely used in supercapacitor [13], lithium ion battery [14], heterogeneous catalysts [16], and so on.

Various morphologies of $\text{Co}(\text{OH})_2$ nanocrystals, such as nanocolumn [17], nanowire [13,18,19], nanocone [11], and nanoflake [2,4,20–22], have been successfully synthesized by different methods. As reported, the reaction temperature, surfactant content, ion concentration and aging time [4,22–24] play important roles in the morphology and size of $\text{Co}(\text{OH})_2$ nanocrystals. $\text{Co}(\text{OH})_2$ nanoflakes and nanoflowers were widely used for supercapacitor and exhibited high specific capacitance due to their pseudo-capacitive behaviors [2,4,21]. However, monodisperse $\text{Co}(\text{OH})_2$ nanowires have rarely been used in the supercapacitor. Due to the

well-defined structure, $\text{Co}(\text{OH})_2$ nanowires may exhibit high capacitance and good stability for practical application.

In this work, nanosized cobalt hydroxides with morphologies of nanocube and nanowire were synthesized via a facile hydrothermal process with CTAB as the soft template. Morphology and particle size can be controlled by the CTAB content and reaction time. The electrochemical capacitive performance of $\text{Co}(\text{OH})_2$ nanowires was evaluated by cyclic voltammetry and galvanostatic charge–discharge measurements. Asymmetric supercapacitor was assembled using $\text{Co}(\text{OH})_2$ nanowires as cathodic electrode and HNO_3 treated activated carbon (NTAC) as anodic electrode. Capacitive performance, cycle life and efficiency of $\text{Co}(\text{OH})_2$ nanowires/NTAC based asymmetric supercapacitor were measured to investigate its potential application in electric vehicles and energy storage.

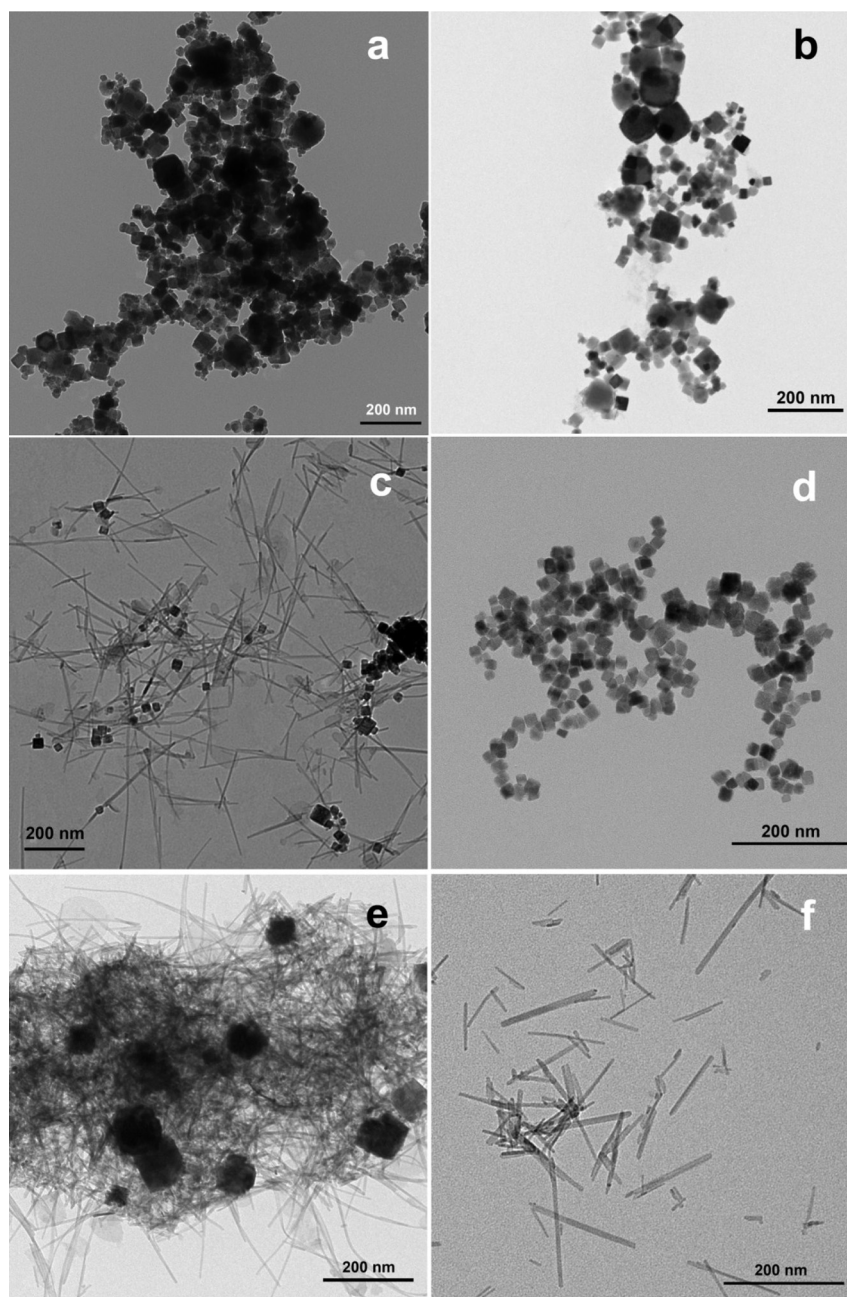


Fig. 1. Typical TEM images of $\text{Co}(\text{OH})_2$ nanocrystals obtained from the hydrothermal process for 4 h at 120 °C with the CTAB content of 2.75 mM (a), 6.90 mM (b), 13.8 mM (c), 69.0 mM (d), 138 mM (e) and 690 mM (f).

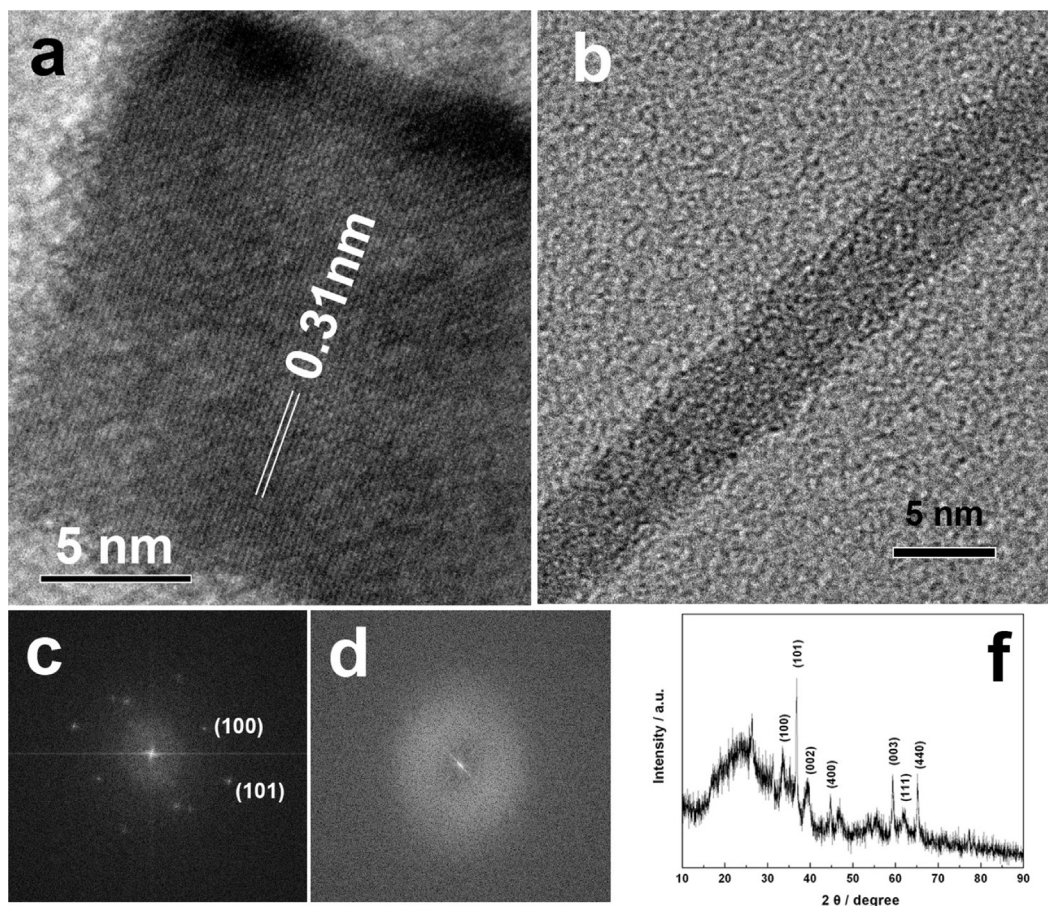


Fig. 2. HRTEM images (a, b) and corresponding FFT images (c, d) of cubic Co(OH)_2 nanocrystal obtained in the CTAB content of 69.0 mM (a, c) and nanowire structured Co(OH)_2 nanocrystal obtained in the CTAB content of 690 mM (b, d). XRD pattern of nanowire structured Co(OH)_2 nanocrystal obtained in the CTAB content of 690 mM (f).

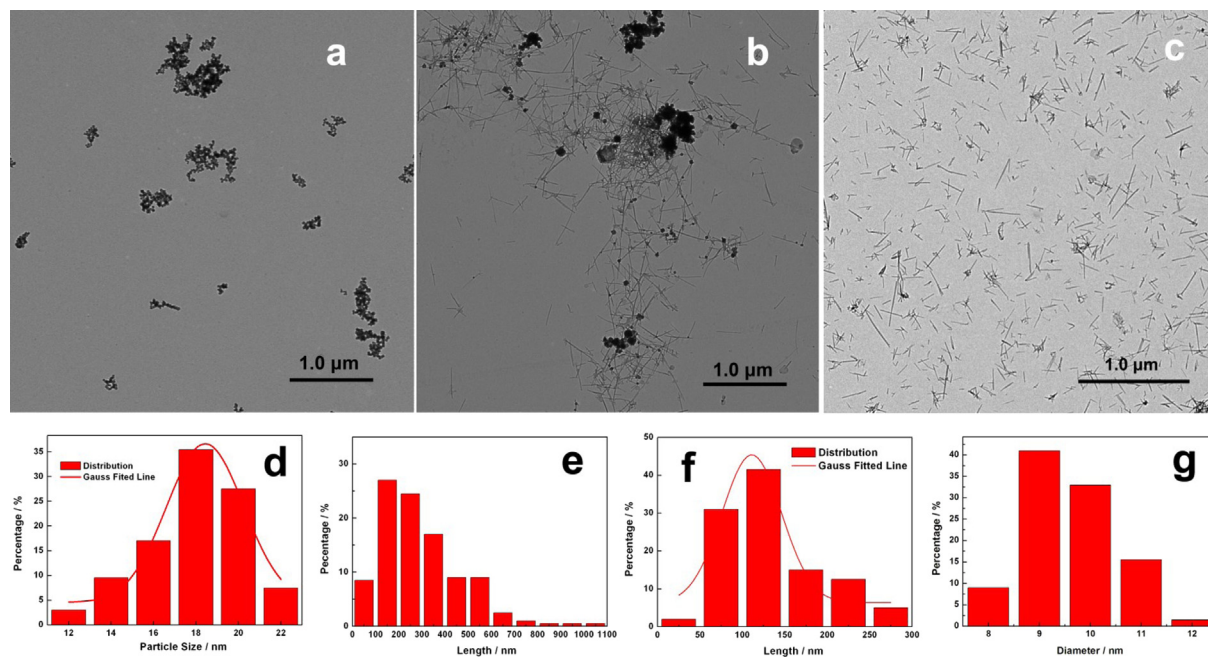


Fig. 3. Low-magnified TEM images (a, b, c) and size distribution histograms (d, e, f, g) of cubic Co(OH)_2 nanocrystal obtained in the CTAB content of 69.0 mM (a, d), nanowire structured nanocrystals obtained in the CTAB content of 13.8 mM (b, e) and 138 mM (c, f, g).

2. Experimental section

2.1. Preparation of cobalt hydroxide nanocrystals

10 mL $\text{Co}(\text{NO}_3)_2$ solution with concentration of 0.17 mol L^{-1} was added into a beaker and diluted with 10 mL deionized water. Designed amount of CTAB was added into the pink solution and heated to be dissolved. The amounts of CTAB were designed as 20, 50, 100, 500, 1000 and 5000 mg, respectively, to investigate the mechanism of morphology control on the cobalt hydroxides. 10 mM KOH solution was added into drop by drop, until the pH value up to about 8. After stirring for 1 h, the mixture solution was transferred into a 100 mL autoclave and reacted in an oven at 120°C for different time (1 h, 2 h, 4 h, 8 h and 23 h). The as-prepared cobalt hydroxides were obtained after separating, washing and drying.

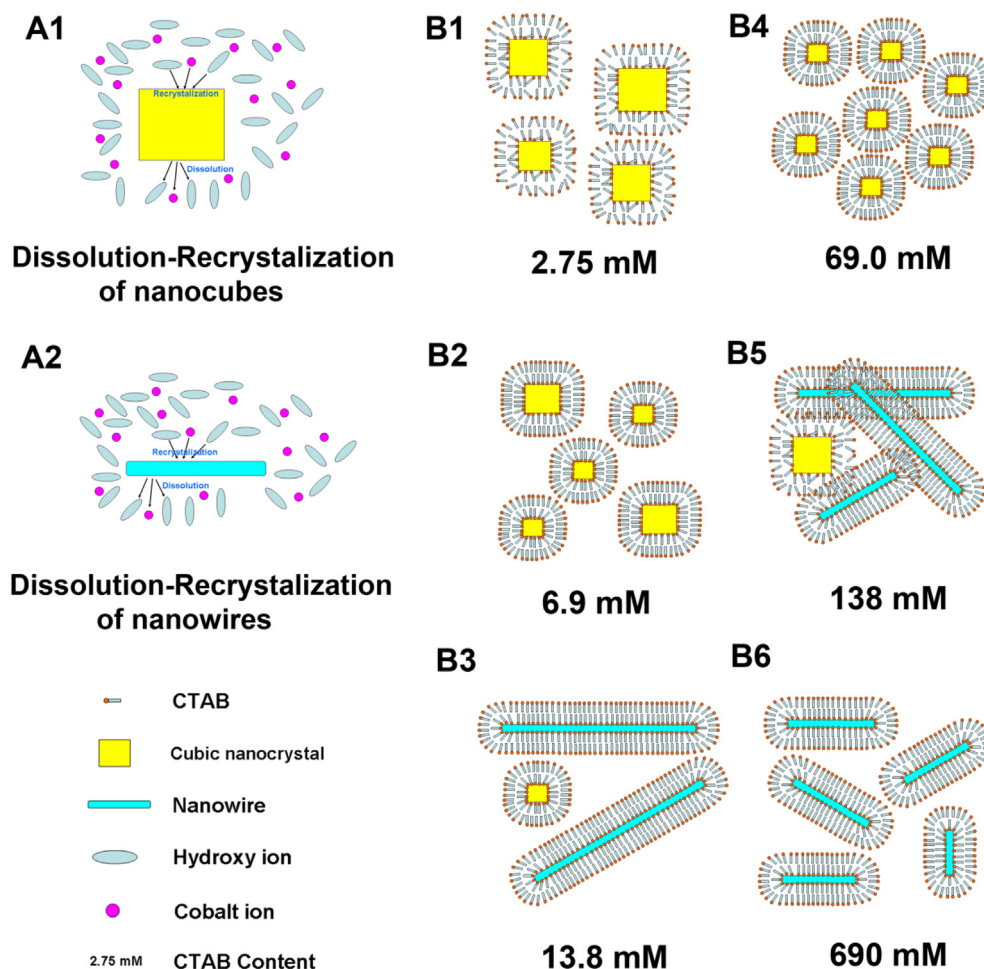
To investigate the effect of morphology on the capacitive behavior, another $\text{Co}(\text{OH})_2$ complex sample was obtained with ammonia as precipitation without CTAB in the synthesis system. 10 mL $\text{Co}(\text{NO}_3)_2$ solution with concentration of 0.17 mol L^{-1} was added into a beaker and diluted with 10 mL deionized water. 2 mL ammonia (35 wt.%) was added drop by drop to obtain the colloid solution. Then the solution was transferred into a 100 mL autoclave and reacted in an oven at 120°C for 4 h. The as-prepared $\text{Co}(\text{OH})_2$ complex sample was obtained after separating, washing and drying.

2.2. Physiochemical characterization of cobalt hydroxides

Morphologies of cobalt hydroxides were characterized by transmission electron microscope (TEM, HT 7700 model, Hitachi Corp., Japan) operating at 100 kV, 10 μA and high-resolution transmission electron microscope (HRTEM, JEM 2010 model, JEOL Ltd. Corp., Japan) operating at 200 kV. The sample was suspended in ethanol to form homogeneous slurry. A drop of slurry was dispersed on the amorphous carbon film supported on Cu grid for TEM and HRTEM analysis.

2.3. Fabrication of electrode and electrochemical measurements

Cyclic voltammetry was carried out on CHI 660A electrochemistry workstation (CH Instrument Corp. USA) with a standard three-electrode electrochemical cell system. The working electrode was prepared as follows: 80 wt.% of cobalt hydroxide sample, 15 wt.% of acetylene black and 5 wt.% of polyvinylidene difluoride (PVDF) were mixed in the ethanol to form a homogeneous slurry. The slurry was coated on the pre-cleaned Pt meshwork and dried in vacuum at 80°C to obtain the working electrode. The active material loading of the electrode is 1.8 mg cm^{-2} . Pt foil ($1 \times 1 \text{ cm}^2$), Hg/HgO electrode and 6.0 M KOH solution were used as counter electrode, reference electrode and electrolyte, respectively. The electrochemical impedance spectrums (EIS) of the electrodes were also carried out by CHI 660A



Scheme 1. Sketch of the effect of CTAB on the morphology of the $\text{Co}(\text{OH})_2$ nanocrystals and nanowires.

workstation. The amplitude is 5 mV and the operating frequency is from 1 Hz to 100 kHz.

Galvanostatic charge–discharge measurements were performed on Land CT 2001A (Land Instrument Corp., Wuhan, China). The specific capacitances of active materials were measured by three-electrode system in 6 M KOH solution. Active materials coated Pt meshwork, large Pt foil ($1 \times 1 \text{ cm}^2$) and Hg/HgO electrode were used as working electrode, counter electrode and reference electrode, respectively. To evaluate the performance for practical application, the asymmetric supercapacitor was assembled with $\text{Co}(\text{OH})_2$ nanowires and HNO_3 treated KB 600 active carbon as cathodic and anodic active materials, respectively. The loading of cathodic and anodic active material are 2.6 mg cm^{-2} and 3.6 mg cm^{-2} , respectively, with the total loading of 6.2 mg cm^{-2} .

3. Results and discussion

Figs. 1 and 2 show the typical TEM images and HRTEM images of the cobalt hydroxides obtained by tuning content of CTAB in the hydrothermal system. The hydrothermal reactions were operated in 120°C for 4 h. As shown, monodisperse nanocubes (Fig. 1d) and nanowires (Fig. 1f) are obtained in the CTAB content of 69.0 mM and 690 mM, respectively. The low magnified TEM images (Fig. 3a, c) and size distribution (Fig. 3d, f) confirm the monodispersity of $\text{Co}(\text{OH})_2$ nanowires and cubic nanocrystals. The mean particle size of cubic nanocrystals is 17.8 nm with distribution from 11 to 20 nm. The average diameter of monodisperse nanowires is 7.3 nm with narrow distribution from 5 to 10 nm.

As shown in the HRTEM image, the regular facets demonstrate single-crystal structure of cubic nanocrystals (Fig. 2a). The facet

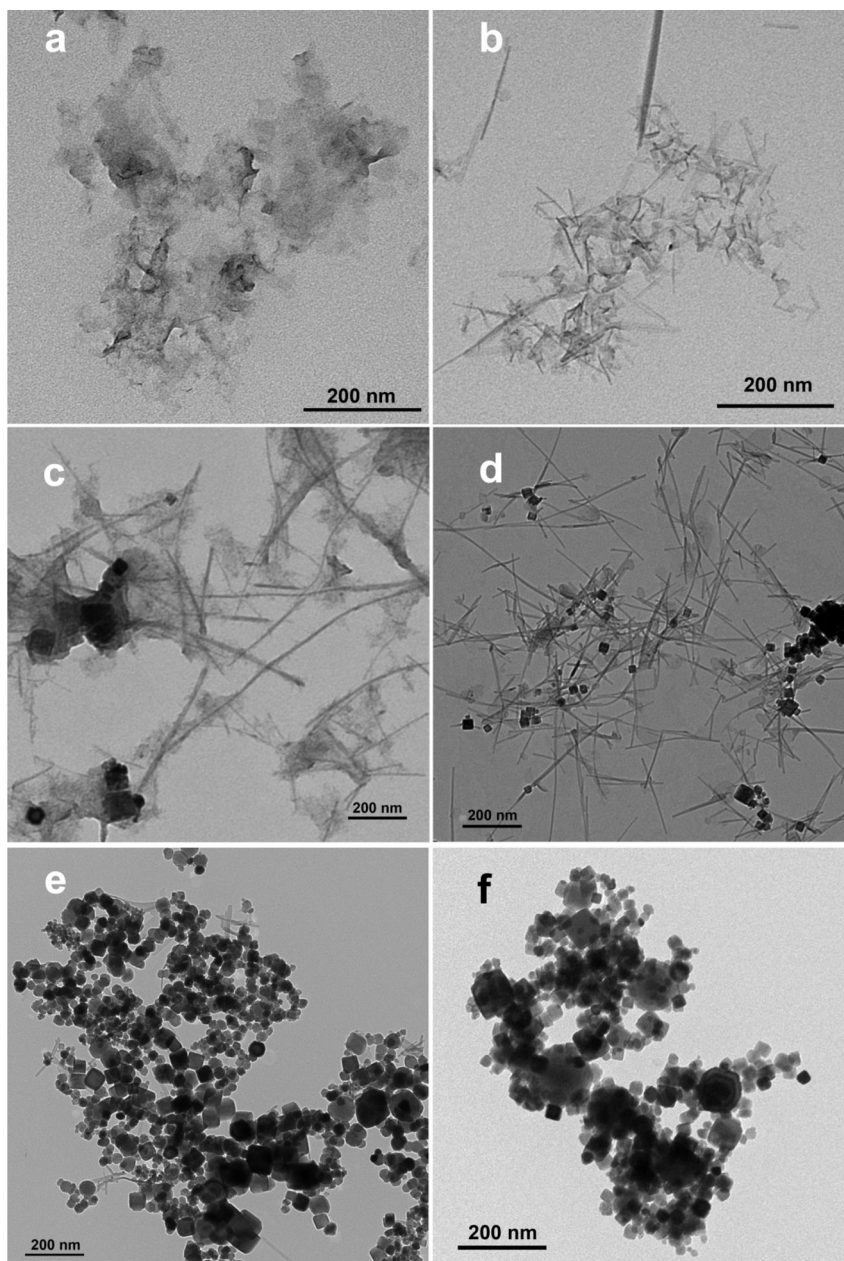


Fig. 4. Morphologies of $\text{Co}(\text{OH})_2$ nanocrystals obtained in the CTAB content of 13.8 mM at non-hydrothermal process (a), hydrothermal reaction with 1 h (b), 3 h (c), 4 h (d), 8 h (e) and 23 h (f).

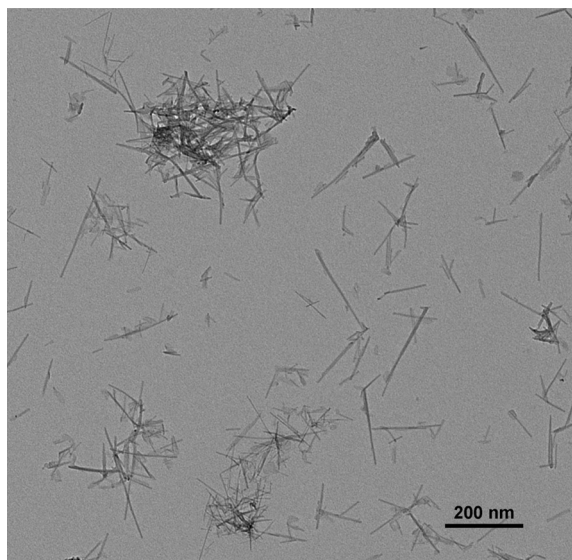


Fig. 5. TEM image of Co(OH)_2 nanowires obtained via hydrothermal process with 69 mM CTAB at 80 °C.

distance is 0.31 nm, which is corresponding to the layer–layer distance of hexagonal β -phase of cobalt hydroxide. The highly crystalline degree of Co(OH)_2 nanocube can be verified by its diffractive dots in the FFT image (Fig. 2c). Although the morphology of

Co(OH)_2 nanowires is well-defined, the clear facets are not observed in the HRTEM image (Fig. 2b). The diffractive ring in the FFT image (Fig. 2d), as well as the wide diffractive peaks in the XRD pattern (Fig. 2d), demonstrates the polycrystalline structure of the Co(OH)_2 nanowires.

To explore the formation mechanism of Co(OH)_2 nanowires, the effect of CTAB content on the morphology of Co(OH)_2 materials is discussed in detail. When CTAB content is as low as 2.75 mM (Fig. 1a), cubic Co(OH)_2 nanocrystals are observed in the TEM images, even though the morphology is not well-defined and the particle size distribution is wide (10 nm ~ 100 nm). With the increase of CTAB content to 6.90 mM, the cubic morphology is more well-defined, and the size of cubic nanocrystals becomes smaller. However, the particle size distribution is still wide (Fig. 1b). It is interesting that ultralong and ultrafine nanowires are observed when CTAB content is 13.8 mM, where smaller well-defined cubic nanocrystals coexist (Fig. 1c). When CTAB content is 69.0 mM, well-defined cubic nanocrystals with monodisperse size are obtained (Fig. 1d). Their size distribution and HRTEM image have been particularly discussed above. As CTAB content increases to 138 mM, the products are composed of interlaced nanowires and irregular cubic nanocrystals (Fig. 1e). When CTAB content is as high as 690 mM, the well-defined nanowires with monodisperse diameter are present (Fig. 1f). Nanowires are observed in the resultant when CTAB contents are 13.8 mM, 138 mM and 690 mM, respectively. However, the morphologies of nanowires obtained with 13.8 mM and 690 mM CTAB are more regular than that obtained with 138 mM CTAB. Moreover, the nanowires obtained with 13.8 mM CTAB exhibit the length from 100 to 1100 nm (Fig. 3b and e), which

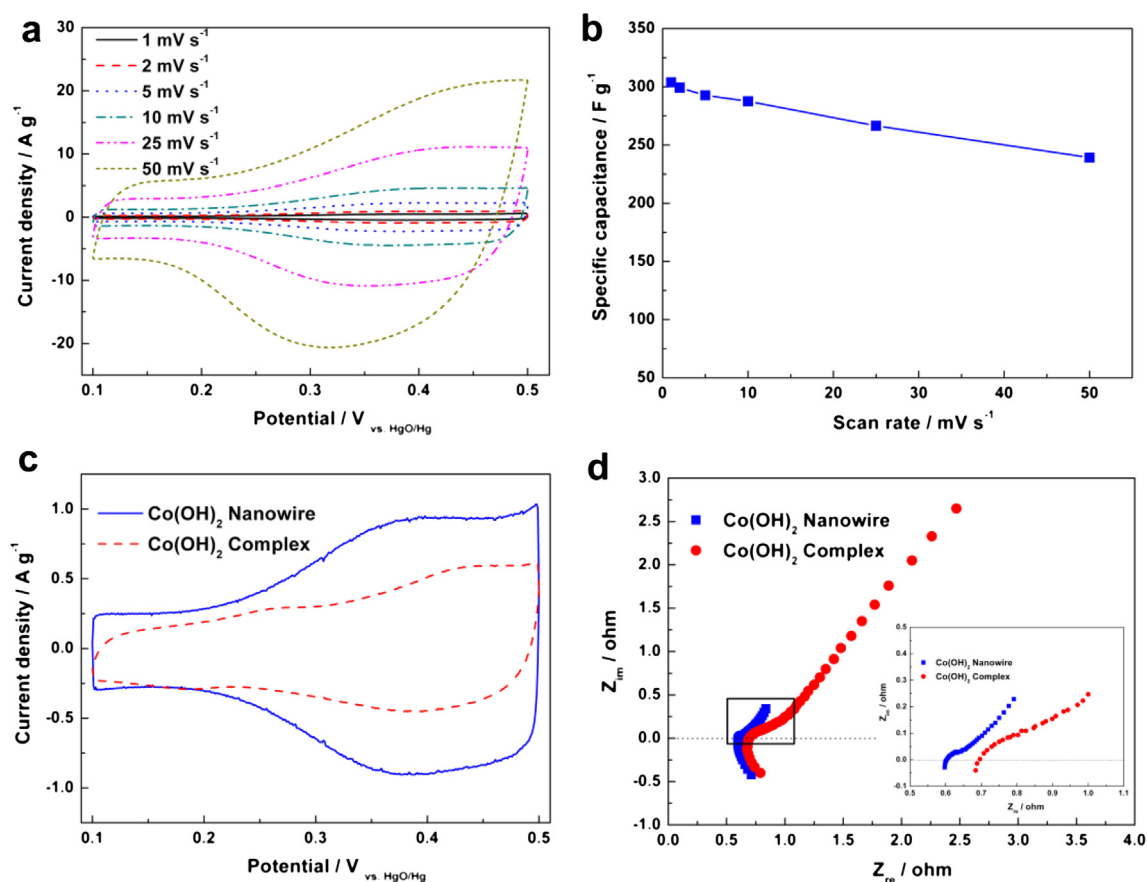


Fig. 6. (a) CV curves of Co(OH)_2 nanowires electrode at different scan rates, (b) Specific capacitances calculated by CV curves at different scan rates, (c) CV curves of Co(OH)_2 nanowires electrode and Co(OH)_2 complex electrode for comparison (d) EIS spectrum of Co(OH)_2 nanowires electrode and Co(OH)_2 complex electrode.

is more longer than that obtained with 690 mM CTAB (50–300 nm).

From the experiment results, a possible mechanism for the effect of CTAB content on the morphology of $\text{Co}(\text{OH})_2$ nanocrystals is suggested as follows (Scheme 1). CTAB, as a typical surfactant, is composed of a hydrophilic head and a hydrophobic organic tail. Due to the hydrophilicity of the $\text{Co}(\text{OH})_2$ precipitation (including floccule, nanocube and nanowire), the hydrophilic head of CTAB trend to adsorb on the surface with the hydrophobic organic tail outward. To reduce the surface energy of system, the surplus CTAB enwraps the adsorbed nanocrystals and nanowires to form micelles, and then the structure of nanocrystals is stabilized. The morphology of CTAB micelles is determined by CTAB content. Furthermore, accelerated dissolution-recrystallization balanceable process of $\text{Co}(\text{OH})_2$ (Eq. (1) and Scheme 1-A1, A2) promotes rearrangement of hydroxide ions and cobalt ions. Therefore, the CTAB content plays important roles in the morphology of $\text{Co}(\text{OH})_2$. When the CTAB content is as low as 2.75 mM, the surplus CTAB, except adsorbed ones, only incompletely enwrap the nanoparticles, leading to the formation of irregular cubic nanocrystals (Fig. 1a and Scheme 1-B1). With the concentration increase, more CTAB trend to adsorb on the surface of nanocrystals, and to form regular micelles, leading to the occurrence of regular and smaller cubic nanocrystals under the CTAB content of 6.9 mM (Fig. 1b and Scheme 1-B2). When the CTAB content continuously increases to 13.8 mM, the spherical micelles transfer to long rod-like micelles. In this case, ultralong and ultrafine nanowires are observed in this CTAB content (Fig. 1c and Scheme 1-B3). When the CTAB concentration is 69.0 mM, which may be higher than its first critical micelle concentration (CMC) but lower than the second CMC [25,26], the surplus CTAB will be suitable for the formation of uniform micelles. Therefore, monodisperse cubic nanocrystals are obtained (Fig. 1d and Scheme 1-B4) in this CTAB content. When CTAB concentrations further increases to 138 mM or 690 mM, the solution system is dominantly composed of short rod-like micelles. Nanowires are the most resultants in the synthesis system (Fig. 1e, f and Scheme 1-B5, B6). Especially, only monodisperse well-defined nanowires are obtained when CTAB content is 690 mM. There are two CTAB contents corresponding to the well-defined nanowires morphology with different length (100–1100 nm and 50–300 nm corresponding to 13.8 mM and 690 mM, respectively). This may be attributed to that there are two CMCs for CTAB [25,26], which corresponding to different micelles.



To further comprehend the formation of $\text{Co}(\text{OH})_2$ nanocubes and nanowires, we also synthesize various $\text{Co}(\text{OH})_2$ samples by tuning the reaction time in the hydrothermal process. Fig. 4 shows the TEM images of $\text{Co}(\text{OH})_2$ samples obtained at different reaction time with 13.8 M CTAB. Based on the dissolution-recrystallization of $\text{Co}(\text{OH})_2$ precipitation and the template role of CTAB, we suggest the formation mechanism of $\text{Co}(\text{OH})_2$ nanocubes and nanowires as follows. $\text{Co}(\text{OH})_2$ floccules are formed by co-precipitation without hydrothermal process (Fig. 4a). Due to the accelerated dissolution-recrystallization of $\text{Co}(\text{OH})_2$ (Scheme 1-A2) by the hydrothermal process via Eq. (1), as well as the directional adsorption of CTAB on the $\text{Co}(\text{OH})_2$ nanocrystals, $\text{Co}(\text{OH})_2$ floccules (Fig. 4a) transfer into irregular nanowires when the hydrothermal reaction is performed for 1 h (Fig. 4b). The nanowires grow longer and more regular when the reaction time is increased to 3 h (Fig. 4c). Furthermore, irregular cubic $\text{Co}(\text{OH})_2$ nanocrystals are observed in this stage. When the reaction time is 4 h, well-defined ultra-long nanowires (100–1100 nm) as well as cubic crystals are observed clearly. When the reaction time increase to 8 h, most of the $\text{Co}(\text{OH})_2$

nanowires transfer into cubic nanocrystals (Fig. 4e). After prolonging the reaction time to 23 h, only well-defined cubic crystals are present in products (Fig. 4f). The transformation from nanowires to cubic nanocrystals may be attributed to the more highly crystalline of nanocubes than that of nanowires, which is confirmed in the HRTEM images (Fig. 2). Another experimental result also confirms this deduction. As shown in Fig. 5, when the reaction is operated in 80 °C and with the CTAB content of 69.0 mM, only $\text{Co}(\text{OH})_2$ nanowires occur. Furthermore, some low crystalline floccules coating on the nanowires are observed in this sample. On the contrary, monodisperse cubic $\text{Co}(\text{OH})_2$ nanocrystals are obtained at 120 °C with the same CTAB content (Fig. 1d). As known, the high temperature aging of $\text{Co}(\text{OH})_2$ crystals promote them transfer into highly crystalline morphology.

Due to the high capacitance and good cycle performance, $\text{Co}(\text{OH})_2$ is a very suitable electrode material for supercapacitors. In this work, capacitive behavior of the as-prepared $\text{Co}(\text{OH})_2$ nanowires electrode is elaborately investigated. Fig. 6a shows the CV curves of $\text{Co}(\text{OH})_2$ nanowires electrode in the 6 M KOH solution at different scan rates. The clearly observed anodic and cathodic peaks should be attributed to the transformation between $\text{Co}(\text{OH})_2$ and

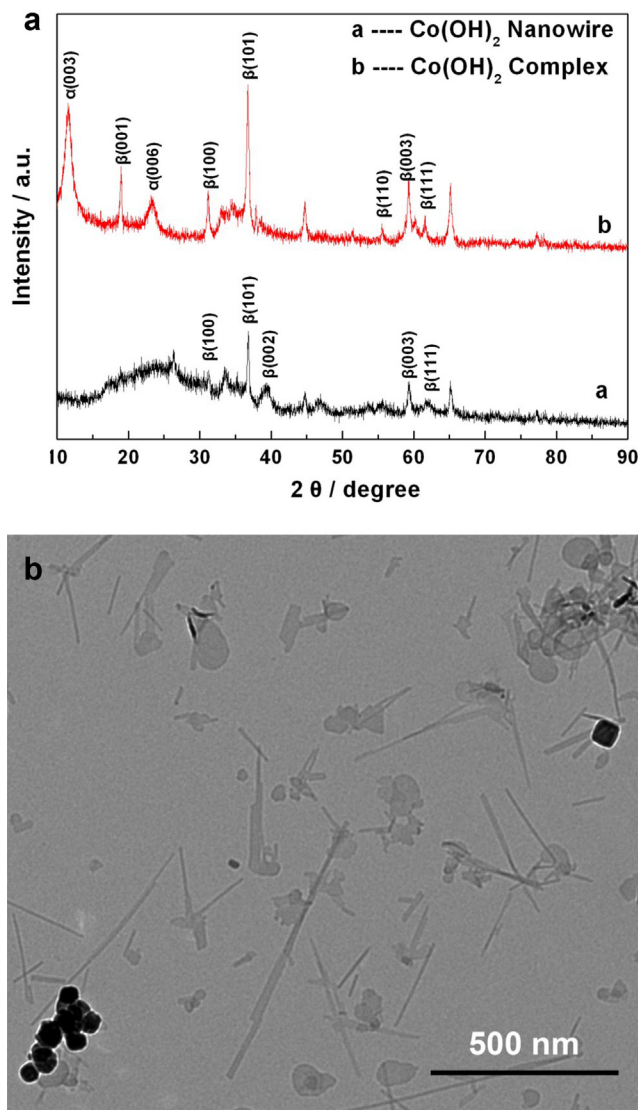
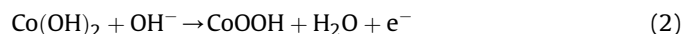


Fig. 7. XRD patterns of $\text{Co}(\text{OH})_2$ samples and the TEM image of $\text{Co}(\text{OH})_2$ complex.

CoOOH presented in Eq. (2) [27,28]. Good symmetry of anodic peak and cathodic peak reveals the reversibility of this reaction, which will contribute the high rate performance of Co(OH)₂ nanowires electrode. The calculation of specific capacitance from CV curve was carried out by Eq. (3), where I was the current, m was the mass of active material, and ΔV was the potential range.



$$C = \int I dt / (m \cdot \Delta V) \quad (3)$$

As shown in Fig. 6b, the specific capacitances of Co(OH)₂ nanowires electrode are 304, 299, 293, 288, 266 and 239 F g⁻¹ at 1, 2, 5, 10, 25 and 50 mV s⁻¹, respectively. The capacitance retention at 50 mV s⁻¹ is 78.6%, demonstrating the good high rate performance of the Co(OH)₂ nanowires electrode. To investigate the effect of morphology on the capacitive performance, Co(OH)₂ complex sample with various morphologies (nanowire, nanocube and nanoflake) are also prepared (described in Experimental section) and measured simultaneously. The XRD pattern and TEM image of Co(OH)₂ complex are shown in Fig. 7. Besides nanowires, nanoflakes and nanocubes are also observed in the Co(OH)₂ complex sample. Moreover, α -phase Co(OH)₂ peaks are present in the XRD pattern of Co(OH)₂ complex besides β -phase. Fig. 6c shows the CV curves of Co(OH)₂ nanowires and Co(OH)₂ complex electrodes at 2 mV s⁻¹. As shown, the peak current density of the Co(OH)₂ complex electrode is markedly lower than that of Co(OH)₂ nanowires electrode. The specific capacitance of Co(OH)₂ nanowires material (299 F g⁻¹) is higher than that of Co(OH)₂ complex

(163 F g⁻¹). The higher capacitance may be ascribed to that the well-defined nanowires are more suitable for the electronic transfer and the ionic transportation, which can be confirmed by the EIS spectrums of the two electrodes. Fig. 6d is the EIS spectrums of the Co(OH)₂ nanowires and Co(OH)₂ complex electrodes. The intersection of EIS plots and real axis represents the ohmic resistance of the electrode [29]. The radius of the high frequency loop is assigned to the charge transfer resistance [30]. As shown, both the ohmic resistance and the charge transfer resistance of Co(OH)₂ complex electrode are larger than those of Co(OH)₂ nanowires electrode, demonstrating that the Co(OH)₂ nanowires material possesses higher electronic conductivity and more suitable structure for the charge transfer.

Galvanostatic charge–discharge measurements are performed to evaluate the supercapacitive performance of Co(OH)₂ nanowires for practical application. Fig. 8a is the charge–discharge curves of Co(OH)₂ nanowires electrode at different current densities. Unlike the linear characteristic of electronic double-layer capacitive (EDLC) electrode, the sloped potential plateaus in the charge and discharge curves reveal the pseudo-capacitive behavior of the Co(OH)₂ nanowires. Good symmetry between the charge curves and the discharge curves demonstrates the good reversibility of the reaction for charge–discharge. Fig. 8b shows the specific capacitance (C_s) and Coulombic efficiency (CE) of the Co(OH)₂ nanowires electrode, which are calculated from Eq. (4) and Eq. (5) [27], where I was the applied current, ΔV was the potential range of charge or discharge, m was the mass of active material, Δt was the time of a charge or discharge process, C_{sc} and C_{sd} were the specific capacitance of charge and discharge process, respectively. The C_s is sensitive to the slope of the discharge curve. Therefore, it is noticed

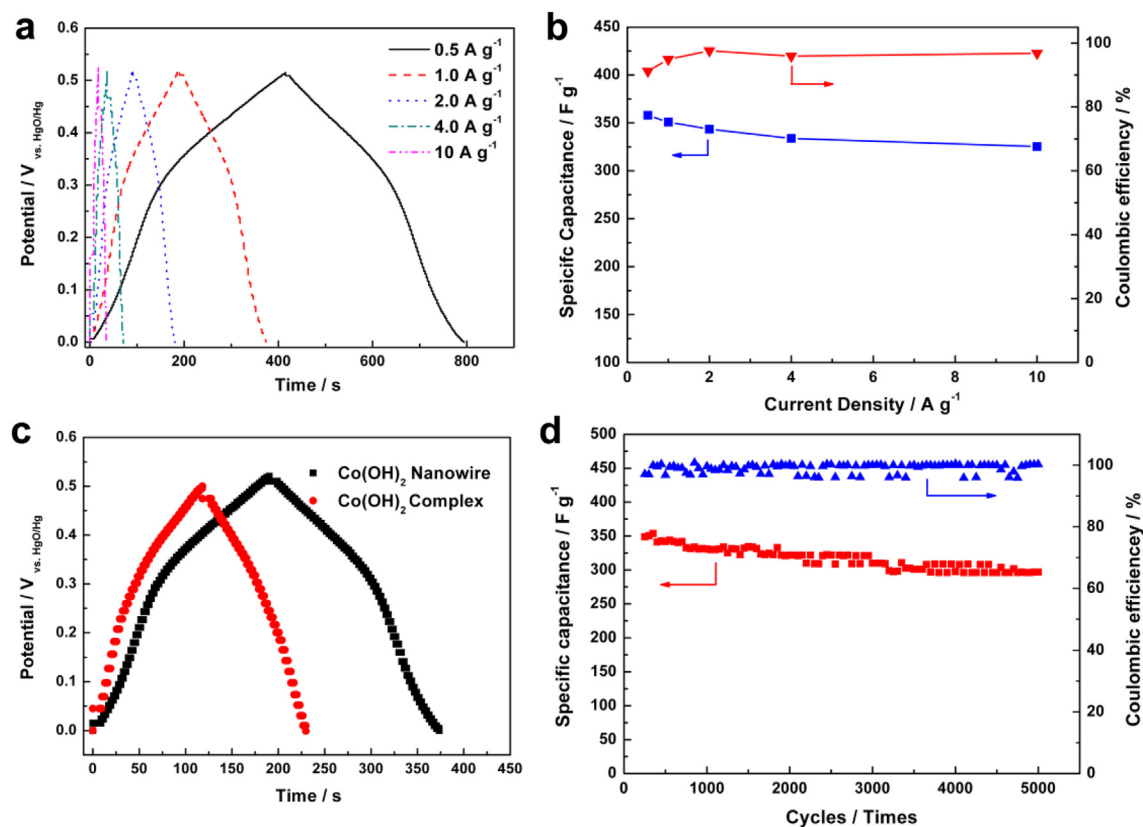


Fig. 8. (a) Charge–discharge curves of Co(OH)₂ nanowires electrode at different current densities, (b) Corresponding specific capacitances and Coulombic efficiencies calculated by charge–discharge data, (c) Charge–discharge curves of Co(OH)₂ nanowire and Co(OH)₂ complex at the charge–discharge current density of 1.0 A g⁻¹ and (d) Cycle life performance of the Co(OH)₂ nanowires electrode at the current density of 2.0 A g⁻¹.

that the calculated C_s here is derived from the mean value of the whole discharge curve based on Eq. (4). The specific capacitances at 0.5, 1, 2, 4, and 10 A g⁻¹ are 358, 351, 344, 334 and 325 F g⁻¹, respectively. The capacitive retention at 10 A g⁻¹ is 90.7%, confirming the high rate capacitive performance of Co(OH)₂ nanowires electrode. All the Coulombic efficiencies are higher than 95% except that at the current density of 0.5 A g⁻¹, which confirms the good reversibility of fast Faradic redox reactions. Fig. 8c is the comparison between the charge–discharge curves of Co(OH)₂ nanowires and Co(OH)₂ complex electrodes. As shown, the Co(OH)₂ nanowires electrode exhibits better performance than the Co(OH)₂ complex counterpart, which only displays 223 F g⁻¹ at 1 A g⁻¹.

$$C_s = \frac{I \cdot \Delta t}{\Delta V \cdot m} \quad (4)$$

$$CE = \frac{C_{sd}}{C_{sc}} \times 100\% \quad (5)$$

The Co(OH)₂ nanowires electrode also exhibits superior cycling stability. Fig. 8d is the cycle life performance of the Co(OH)₂ nanowires electrode. After 5000 charge–discharge cycles at 2 A g⁻¹, the specific capacitance retention is 86.3%. It is better than the other oxide or hydroxide electrodes in literature [11,31–34]. The high cycle performance may be attributed to the stable structure of well-defined Co(OH)₂ nanowires. Furthermore, the Co(OH)₂ nanowires electrode displays high Coulombic efficiency (>95%, red

Table 1

Charge–discharge properties of Co(OH)₂-nanowire/NTAC-based asymmetric supercapacitor calculated by charge–discharge curves.

Discharge current (A)	1.2	3.1	6.2	12.3
Capacitance (F g ⁻¹)	38.9	31.5	29.9	29.4
Coulombic efficiency (%)	92.6	96.5	95.0	95.0
Energy density (Wh kg ⁻¹)	13.6	12.6	12.9	13.1
Power density (W kg ⁻¹)	153	449	970	1885

triangle in Fig. 8d), which is in good agreement with the good reversibility of the charge–discharge process.

Asymmetric supercapacitor is assembled using Co(OH)₂ nanowire as cathodic electrode and HNO₃ treated activated carbon (NTAC) materials (KetjenBlack EC 600J, AzkoNobel Corp., Netherlands) as anodic electrode. The specific capacitance of the NTAC is 154 F g⁻¹ operating around -0.1 ~ -1.0 V at the current density of 0.5 A g⁻¹. The charge–discharge curves of Co(OH)₂-nanowires/NTAC-based asymmetric supercapacitor are shown in Fig. 9a and the performance data are collected in Table 1. The voltage of supercapacitor reaches up to 1.6 V. Pseudo-capacitive characteristic is clearly observed. The charge and discharge curves are nearly mirrored asymmetry, which reveals the good redox reversibility for the anodic and cathodic processes. Calculated by the total mass of both cathodic and anodic active materials, the specific capacitances at the discharge current of 1.2, 3.1, 6.2, and 12.3 mA are 38.9, 31.5, 29.9 and 29.4 F g⁻¹, respectively. It is clearly larger than that of conventional AC-based symmetric capacitors (~20 F g⁻¹) [35]. Fig. 9b shows the Ragone plots of Co(OH)₂-nanowires/NTAC-based asymmetric capacitor. The as-prepared asymmetric capacitor with a cell voltage of 1.6 V can exhibit an energy density of 13.6 Wh kg⁻¹ at the power density of 153 W kg⁻¹, and still retains 13.1 Wh kg⁻¹ at the power density of 1.88 kW kg⁻¹. This energy density is much higher than that of commercial symmetric electric double layer capacitors (EDLCs, 3–4 Wh kg⁻¹ at 3–4 kW kg⁻¹) [36,37]. Furthermore, the asymmetric supercapacitor displays high Coulombic efficiency (>90%) and energy efficiency (>80%), which are important for the practical application of supercapacitor.

4. Conclusions

In summary, monodisperse cobalt hydroxide cubic nanocrystals and nanowires are synthesized by a facile hydrothermal process. Morphology of cobalt hydroxide can be easily tuned by the CTAB content and reaction time. The template effect of CTAB and the dissolution-recrystallization of Co(OH)₂ play important roles in the morphology control of Co(OH)₂ nanocrystals and nanowires. The obtained Co(OH)₂ nanowires, which exhibit good capacitive performance and excellent cycle life, are ideal active materials for supercapacitors. The Co(OH)₂ nanowires based electrode exhibits high capacitance of 358 F g⁻¹ at the discharge current density of 0.5 A g⁻¹, and retains 325 F g⁻¹ even at 10 A g⁻¹. The specific capacitance of Co(OH)₂ nanowire electrode still retains 86.3% after 5000 charge–discharge cycles at 2.0 A g⁻¹. Asymmetric supercapacitor assembled with Co(OH)₂ nanowires based cathode and NTAC based anode exhibits specific capacitance of 29.4–38.9 F g⁻¹, which are larger than that of conventional activated carbon based symmetric supercapacitor. The energy density of as-prepared asymmetric supercapacitor is 13.6 Wh kg⁻¹ at the power density of 153 W kg⁻¹, and still retains 13.1 Wh kg⁻¹ at the power density of 1.88 kW kg⁻¹. The as-prepared asymmetric supercapacitor displays high and stable Coulombic efficiency (>90%), as well as high energy efficiency (>80%). High performances, long cycle life and high efficiencies of Co(OH)₂ nanowires based electrode, as well as

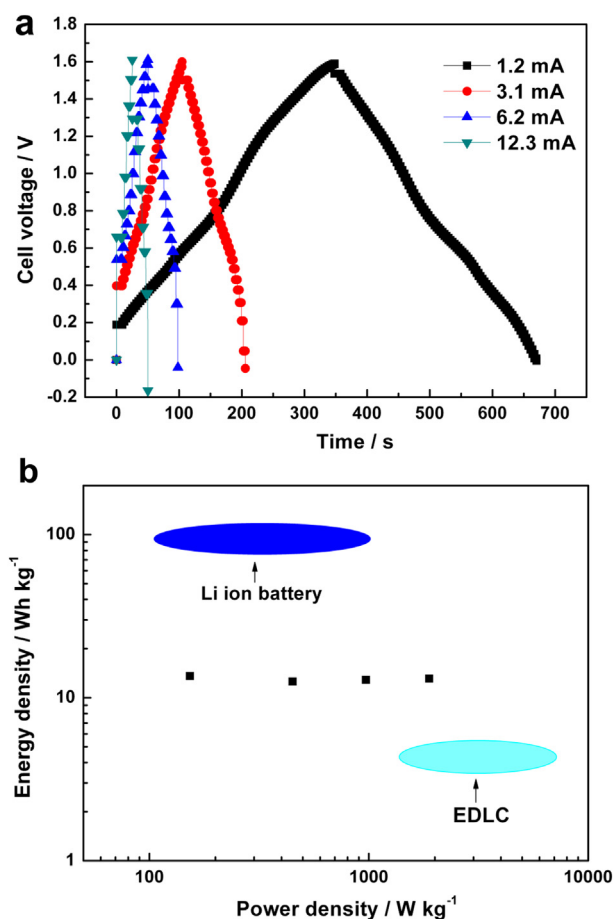


Fig. 9. (a) Charge–discharge curves and (b) Ragone plots for energy density and power density of Co(OH)₂-nanowires/NTAC-based asymmetric supercapacitor (calculated by the total active materials).

Co(OH)₂-nanowires/NTAC based asymmetric supercapacitor boost their potential applications in electric vehicles and electrochemical energy storage.

Acknowledgments

This work was supported by Natural Science Foundation of Hebei Province (No. B2013203199 and B2012203043), China Postdoctoral Science Foundation (No. 2012M520597) and Key Technology Research and Development Program of Qinhuangdao (No. 2012021A072). Furthermore, this project was supported by State Key Laboratory of Advanced Technology for Material Synthesis and Processing (Wuhan University of Technology) (No. 2013-KF-11).

References

- [1] P. Li, D. Wang, Q. Peng, Y. Li, *Cryst. Growth Des.* 13 (2013) 1949–1954.
- [2] C. Yuan, L. Hou, D. Li, L. Shen, F. Zhang, X. Zhang, *Electrochim. Acta* 56 (2011) 6683–6687.
- [3] Y. Wang, H. Wang, X. Wang, *Electrochim. Acta* 92 (2013) 298–303.
- [4] T. Zhao, H. Jiang, J. Ma, J. Power Sources 196 (2011) 860–864.
- [5] P. Elumalai, H.N. Vasan, N. Munichandraiah, J. Power Sources 93 (2001) 201–208.
- [6] D. Song, Y. Wang, Q. Wang, Y. Wang, L. Jiao, H. Yuan, J. Power Sources 195 (2010) 7115–7119.
- [7] J. Wu, D. Zhang, Y. Wang, Y. Wan, B. Hou, J. Power Sources 198 (2012) 122–126.
- [8] M. Jafarian, M.G. Mahjani, H. Heli, F. Gopal, H. Khajehsharifi, M.H. Hamed, *Electrochim. Acta* 48 (2003) 3423–3429.
- [9] Y. Asano, T. Komatsu, K. Murashiro, K. Hoshino, J. Power Sources 196 (2011) 5215–5222.
- [10] T. Wu, C.Z. Yuan, *Mater. Lett.* 85 (2012) 161–163.
- [11] F. Cao, G.X. Pan, P.S. Tang, H.F. Chen, J. Power Sources 216 (2012) 395–399.
- [12] M. Vidotti, M.R. Silva, R.P. Salvador, S.I. Córdoba de Torresi, L.H. Dall'Antonia, *Electrochim. Acta* 53 (2008) 4030–4034.
- [13] F. Zhang, C. Yuan, X. Lu, L. Zhang, Q. Che, X. Zhang, J. Power Sources 203 (2012) 250–256.
- [14] W.Y. Li, L.N. Xu, J. Chen, *Adv. Funct. Mater.* 15 (2005) 851–857.
- [15] L. Hu, Q. Peng, Y. Li, J. Am. Chem. Soc. 130 (2008) 16136–16137.
- [16] G. Wang, D. Cao, C. Yin, Y. Gao, J. Yin, L. Cheng, *Chem. Mater.* 21 (2009) 5112–5118.
- [17] Y. Shao, J. Sun, L. Gao, J. Phys. Chem. C. 113 (2009) 6566–6572.
- [18] W.E. Mahmoud, F.A. Al-Agel, J. Phys. Chem. Solids 72 (2011) 904–907.
- [19] W.E. Mahmoud, T. Al-Harbi, *Mater. Lett.* 65 (2011) 1986–1988.
- [20] L. Tian, K. Huang, Y. Liu, S. Liu, J. Solid State Chem. 184 (2011) 2961–2965.
- [21] L.B. Kong, J.W. Lang, M. Liu, Y.C. Luo, L. Kang, J. Power Sources 194 (2009) 1194–1201.
- [22] J.R. Neilson, B. Schwenzer, R. Seshadri, D.E. Morse, *Inorg. Chem.* 48 (2009) 11017–11023.
- [23] J. Feng, H. Zeng, *Chem. Mater.* 15 (2003) 2829–2835.
- [24] J.B. Nelson, A.M. Davis, D.M. Wellman, *Inorg. Chem.* 48 (2009) 10857–10858.
- [25] T.Q. Liu, R. Guo, M. Shen, W.L. Yu, *Acta Phys. Chim. Sin.* 12 (1996) 337–340.
- [26] H.J. Lu, C. Chen, H.T. Guo, et al., *Acta Chim. Sin.* 64 (2006) 2437–2441.
- [27] M. Aghazadeh, H.M. Shiri, A.A.M. Barmi, *Appl. Surf. Sci.* 273 (2013) 237–242.
- [28] C. Zhao, X. Wang, S. Wang, Y. Wang, Y. Zhao, W. Zheng, *Int. J. Hydrogen Energy* 37 (2012) 11846–11852.
- [29] F.Q. Liu, B.L. Yi, D.M. Xing, J.R. Yu, Z.J. Hou, Y.Z. Fu, J. Power Sources 124 (2003) 81–89.
- [30] M. Eikerling, A.A. Kornyshev, J. Electroanal. Chem. 475 (1999) 107–123.
- [31] Z. Tang, C. Tang, H. Gong, *Adv. Funct. Mater.* 22 (2012) 1272–1278.
- [32] X. Zhang, P. Yu, H. Zhang, D. Zhang, X. Sun, Y. Ma, *Electrochim. Acta* 89 (2013) 523–529.
- [33] G.X. Pan, X. Xia, F. Cao, P.S. Tang, H.F. Chen, *Electrochim. Acta* 63 (2012) 335–340.
- [34] J. Yan, E. Khoo, A. Sumboja, P.S. Lee, *ACS Nano* 4 (2010) 4247–4255.
- [35] Y.G. Guo, J.S. Hu, L.J. Wan, *Adv. Mater.* 20 (2008) 2878–2887.
- [36] B.E. Conway, *Electrochemical Supercapacitors-Scientific Fundamentals and Technological Applications*, Kluwer Academic/Plenum Publisher, New York, 1999.
- [37] P.C. Chen, G. Shen, Y. Shi, H. Chen, C. Zhou, *ACS Nano* 4 (2010) 4403–4410.